Article

Not peer-reviewed version

Dual-Functional Magnetic Nano-Silver/Coal Fly Ash Composite for Simultaneous Degradation of Methyl Orange and Broad-Spectrum Pathogen Disinfection in Wastewater

Lei Gong *, Jiaxin Li, Rui Jin, Menghao Li, Jiajie Peng, Jie Zhu *

Posted Date: 7 July 2025

doi: 10.20944/preprints202507.0483.v1

Keywords: Nano-silver composite; Magnetized coal fly ash; Antibacterial activity; Methyl orange degradation; Sustainable wastewater treatment

 doi:10.20944/preprints202507.0483.v1

Article

Dual-Functional Magnetic Nano-Silver/Coal Fly Ash Composite for Simultaneous Degradation of Methyl Orange and Broad-Spectrum Pathogen Disinfection in Wastewater

Lei Gong [1,2,*], Jiaxin Li [2], Rui Jin [2], Menghao Li [3], Jiajie Peng [3] and Jie Zhu [1,*]

[1] National-Local Joint Engineering Research Center of Biomass Refining and High-Quality Utilization, Institute of Urban & Rural Mining, Changzhou University, 213164, Jiangsu Province, China

[2] School of Petrochemical Engineering, Changzhou University, 213164, Jiangsu Province, China

[3] School of Environment Science and Engineering, Changzhou University, 213164, Jiangsu Province, China

* Correspondence: gonglei@cczu.edu.cn (L.G.); zhujie@cczu.edu.cn (J.Z.)

Abstract

In this study, we report the development of a novel magnetized coal fly ash-supported nano-silver composite (AgNPs/MCFA) for dual-functional applications in wastewater treatment: efficient degradation of methyl orange (MO) dye and broad-spectrum antibacterial activity. The composite was synthesized via a facile impregnation-reduction-sintering route, utilizing sodium citrate as both a reducing and stabilizing agent. The AgNPs/MCFA composite was systematically characterized through multiple analytical techniques, including Fourier transform infrared spectroscopy (FTIR), scanning electron microscopy (SEM) and transmission electron microscopy (TEM), X-ray diffraction (XRD), and vibrating sample magnetometry (VSM). Results confirmed the uniform dispersion of AgNPs (average size: 13.97 nm) on the MCFA matrix, with chemical bonding (Ag-O-Si) enhancing stability. Under optimized conditions (0.5 g·L^{-1} $AgNO_3$, 250 °C sintering temperature, and 2 h sintering time), AgNPs/MCFA exhibited exceptional catalytic performance, achieving 99.89% MO degradation within 15 min (pseudo-first-order rate constant k_a=0.3133 min^{-1}) in the presence of $NaBH_4$. The composite also demonstrated potent antibacterial efficacy against *Escherichia coli* (MIC=0.5 mg·mL^{-1}) and *Staphylococcus aureus* (MIC=2 mg·mL^{-1}), attributed to membrane disruption, intracellular content leakage, and reactive oxygen species generation. Remarkably, AgNPs/MCFA retained >90% catalytic and antibacterial efficiency after five reuse cycles, enabled by its magnetic recoverability. By repurposing industrial waste (coal fly ash) as a low-cost carrier, this work provides a sustainable strategy to mitigate nanoparticle aggregation and environmental risks while enhancing multifunctional performance in water remediation.

Keywords: nano-silver composite; magnetized coal fly ash; antibacterial activity; methyl orange degradation; sustainable wastewater treatment

1. Introduction

The sustainable development of human society is increasingly challenged by persistent global pollution, with industrial effluent discharge emerging as a critical contributor. Among various industrial contaminants, textile printing and dyeing wastewater stands out for its formidable treatment challenges, characterized by high volume, elevated organic pollutant concentrations, complex chemical composition, and significant fluctuations in water quality parameters [1]. Azo dyes, such as methyl orange (MO) and its derivatives, are especially problematic due to their intricate molecular structures and exceptional stability, which render them highly resistant to microbial degradation and enable their long-term persistence in ecosystems [2]. Alarmingly, these recalcitrant

 doi:10.20944/preprints202507.0483.v1

compounds can undergo secondary transformations into more complex derivatives, potentially augmenting their mutagenic and carcinogenic properties, thereby posing severe risks to ecological balance and human health [3].

Current strategies for dye removal, including adsorption, reverse osmosis, membrane separation, and chemical oxidation, are hindered by substantial limitations, such as exorbitant operational costs, incomplete organic dye degradation, and inadequate addressing of coexisting microbial hazards [4,5]. The heterogeneous and variable nature of industrial wastewater further fosters the proliferation of harmful microorganisms, including pathogenic strains, which exacerbate risks to environmental and public health. These challenges underscore the urgent need for cost-effective, efficient and multifunctional technologies capable of concurrently mitigating dye contamination and microbial threats in wastewater systems.

Nanoparticles, particularly silver nanoparticles (AgNPs), have attracted significant attention due to their distinctive physicochemical properties and versatile applications in antimicrobial therapy, catalysis, sensing, and materials science [6]. Their pronounced antimicrobial efficacy, stemming from the ability to disrupt microbial cell membranes and inhibit genetic material synthesis, offers a promising solution to combat antibiotic resistance and multidrug-resistant microbial strains prevalent in industrial and medical settings [7]. For instance, Singh et al. reported dose-dependent antimicrobial activity of AgNPs, achieving substantial growth inhibition of bacteria at concentrations between 0.5-2 $mg \cdot mL^{-1}$, highlighting their therapeutic potential in managing bacterial infections [8]. Korkmaz et al. further reported that AgNPs synthesized using *Ficus carica* leaf extract exhibited potent antibacterial and anticancer activities, underscoring their biocompatible and multifunctional nature [9]. Eslam et al. showed AgNPs derived from *Haplophyllum tuberculatum* extract possessed broad-spectrum antibacterial activity against wastewater pathogens (e.g., *Escherichia coli and Staphylococcus aureus*), when synthesized with sodium borohydride, facilitated efficient catalytic degradation of dyes via intermediate organic molecules into environmentally benign products [10,11]. However, the high surface energy of AgNPs often leads to aggregation, compromising their catalytic performance. To address this, supported nanoparticle systems, immobilizing AgNPs on substrates or within composite matrices, have been developed, enhancing stability and reactivity for applications in water treatment, including dye degradation and antimicrobial processes [12–15].

Coal fly ash (CFA), a byproduct of coal-fired power plants, represents a critical industrial waste with global annual production reaching millions of tons, driven by escalating energy demands [16]. The substantial accumulation and restricted recycling of CFA not only present considerable threats to the environment but also pose significant risks to human health. This urgent situation calls for the development and implementation of novel and innovative strategies to effectively utilize the resources at hand [17]. Composed primarily of SiO_2 and Al_2O_3, with trace metal ions and amorphous phases, CFA offers notable advantages: low cost, thermal stability, and superior surface and physicochemical properties, making it a viable silicon-aluminum raw material for zeolite synthesis and a versatile support for catalytic applications [18–21]. Its large surface area and ion-exchange capacity render CFA an ideal substrate for immobilizing nanoparticles, enabling the fabrication of composites with retained antibacterial and catalytic properties for water purification [22,23]. Recent studies have demonstrated CFA-based composites, such as alkaline/zinc-activated fly ash (A-FA/Zn) and fly ash cenosphere-supported photocatalysts (Ag-TON/FAC), exhibit efficient dye adsorption, photocatalytic degradation, and antibacterial activity [24–26]. However, the direct loading of AgNPs onto CFA for simultaneous microbial decontamination and dye degradation remains unexplored, presenting an unaddressed research gap.

In this study, we report the development of a novel AgNPs/magnetized coal fly ash (MCFA) composite via an impregnation-reduction-sintering route, aiming to integrate the antimicrobial and catalytic properties of AgNPs with the structural advantages of MCFA. The composite was comprehensively characterized to evaluate its structural, morphological, and physicochemical properties. Its antibacterial efficacy was evaluated against Gram-negative (*Escherichia coli*) and Gram-positive (*Staphylococcus aureus*) bacteria, while its catalytic performance was assessed via the

 doi:10.20944/preprints202507.0483.v1

degradation of methyl orange (MO), a model azo dye. Mechanistic insights into the antibacterial and catalytic processes were proposed based on the experimental results, offering a foundational framework for developing cost-effective, multifunctional wastewater treatment materials.

2. Results and Discussion

2.1. Characterization of AgNPs/MCFA

From the SEM diagram (Figure S1), it was evident that CFA exhibited a relatively uniform spherical shape and possesses a smooth surface. Acidification led to the removal of impurities from CFA, resulting in the formation of numerous new microstructures, thereby enhancing its ion exchange and adsorption capabilities. In addition, the magnetic particles synthesized by the co-precipitation method exhibit uniform growth on the surface of CFA and strong adhesion. The pretreatment with CFA facilitates the creation of a large number of anchoring sites for AgNPs, allowing for an even distribution of AgNPs across the pore surfaces of MCFA. The presence of small pores promoted controlled release mechanisms for nanoparticles, thereby enhancing their sustained antibacterial and catalytic efficacy [30].

TEM analysis (Figure S2) confirmed the effectiveness of the loading method in achieving a uniform dispersion and controlled distribution of nanoparticles across the CFA surface. The small pore structure of the CFA served as a nanoreactor, spatially confining the nucleation sites during Ag reduction and enabling precise size regulation. Consequently, the synthesized AgNPs exhibited a narrow size distribution with an average diameter of 13.97 nm. High-resolution TEM (HRTEM) imaging revealed well-defined lattice fringes of AgNPs both deposited on and embedded within the CFA matrix. The measured interplanar spacing of 0.224 nm corresponded to the Ag(111) crystallographic plane but showed a contraction of 0.012 nm compared to the standard value (0.236 nm). This deviation suggested lattice compression, likely induced by interfacial Ag-O-Si bonding between the nanoparticles and the silica-rich CFA substrate.

The characterization of the AgNPs/MCFA composites was conducted using FT-IR spectroscopy, as illustrated in Figure S3. In contrast to CFA, MCFA displayed characteristic bands that indicate the magnetization process did not introduce additional intensity bands; rather, it reflected a physical doping process without generating new functional groups. The broad absorption peaks at 3420 cm^{-1} and 3160 cm^{-1} are attributed to the strong stretching vibration of O-H bonds. Furthermore, the absorption peak at 1620 cm^{-1} associated with the carboxyl group ($-COO^-$). The hydroxyl group (-OH) in sodium citrate exhibited reductive properties, enabling the reduction of silver ions into nano-sized silver particles while simultaneously undergoing oxidation to form carboxyl compounds. Additionally, trisodium citrate can complex with silver ions to create a coating layer on the surface of AgNPs, thereby enhancing their dispersion and stability [31]. The peak at 1370 cm^{-1} was likely attributable to the symmetric stretching vibration of nitrate ions (NO_3^-) [32], further confirming the presence of NO_3^- on the surface of AgNPs. At 1100 cm^{-1}, the peak was attributed to the asymmetric stretching vibration of Si-O-Si bonds within CFA [33]. Following there was a noticeable decrease in intensity for this peak along with an emergence of a new Ag-O-Si peak emerges at 470 cm^{-1} [34]. This observation suggested that the interaction between AgNPs and CFA involved more than mere physical adsorption; they also entailed chemical bond formation with the CFA surface.

The XRD analysis confirmed the presence of AgNPs/MCFA composites, as depicted in the Figure S4. The graph clearly showed a broad diffraction peak appears at approximately 25°, indicating a significant abundance of amorphous vitreous bodies within CFA [35]. These structural characteristics confer high hydrophilicity, surface activity, and adsorption properties to CFA. Following modification, a rightward shift was observed, signifying an increase in diffraction angle, decrease in crystal plane spacing, and the introduction of lattice defects. Seven characteristic peaks corresponding to Fe_3O_4 nanoparticles (2θ=30.3°, 35.5°, 43.3°, 53.4°, 57.3°,63.8°, and 74.2°) were identified in MCFA, which correspond to (220), (311), (400), (422), (511), and (440) crystal faces based on standard spectrum of Fe_3O_4. Additionally, four minor peaks at 38.1°, 44.5°, 64.3°, and 78.1°

 doi:10.20944/preprints202507.0483.v1

correspond to (111), (200), (220) and (311) crystal faces respectively according to the standard spectrum for AgNPs with face-centered cubic structure. In conclusion, it can be inferred from the XRD pattern that the CFA was magnetized and effectively loaded with AgNPs.

The VSM curve illustrated in the Figure S5 demonstrates the remarkable superparamagnetism of AgNPs/MCFA, with a saturation magnetization of 68.7 emu·g^{-1}, which was 11.3 emu·g^{-1} lower than that of Fe_3O_4. This reduction can be attributed to the encapsulation effect of CFA, resulting in a weakening of the magnetic properties. In aqueous environments, AgNPs/MCFA tend to settle at the bottom when left undisturbed; however, upon introducing a magnet to the tube wall, a significant number of magnetic particles rapidly accumulated on the side with the magnet, facilitating in-situ separation. Consequently, AgNPs/MCFA showed great potential for rapid recovery and repeated utilization in water treatment applications.

2.2. Effects of $AgNO_3$ Concentration on the Antibacterial Ability

The concentration of $AgNO_3$ had a significant impact on the antibacterial properties of AgNPs, as demonstrated in Figure 1(a). The antibacterial efficacy of AgNPs/MCFA against *E. coli* was more pronounced than that against *S. aureus*. This difference can be attributed to the greater susceptibility of the outer membrane of *E. coli* to disruption by AgNPs/MCFA, in contrast to the thick peptidoglycan layer present in *S. aureus*, similar findings were reported by Waldo-Mendoza et al. in their study [36]. Furthermore, the antibacterial performance of the AgNPs/MCFA against both *E. coli* and *S. aureus* progressively improved with an increase in $AgNO_3$ concentration from 0.1 to 0.5 g·L^{-1}. However, during the reduction reaction at elevated concentrations of $AgNO_3$, a substantial number of nuclei for AgNPs were formed, leading to localized supersaturation conditions. This phenomenon promoted the formation of numerous small particles and resulted in an uneven distribution of AgNPs on the surface of MCFA, thereby diminishing its antimicrobial efficacy. Consequently, it was determined that the optimal concentration of $AgNO_3$ for synthesizing AgNPs on the surface of MCFA was 0.5 g·L^{-1}.

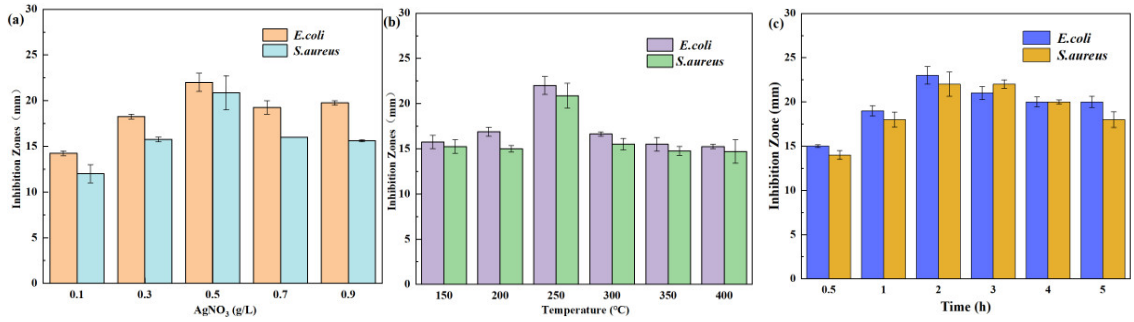

Figure 1. Effect of different $AgNO_3$ concentrations (a), sintering temperature (b), and sintering time (c) on antibacterial properties.

2.3. Sintering Temperature and Sintering Time on the Antibacterial Ability

The impact of high-temperature sintering and sintering time on the antibacterial efficacy of the AgNPs/MCFA was examined, with the results illustrated in Figure 1(b)-(c). High-temperature sintering facilitated a more secure anchoring of AgNPs onto the surface of MCFA, thereby preventing peeling or scattering during application and enhancing long-term performance. The thermal sintering process promoted inter-particle bonding among silver powder particles, leading to a densely interconnected structure. An optimal combination of sintering temperature and time can enhance the crystallization and stability of AgNPs, further optimizing their antibacterial properties. At a sintering temperature of 250 °C for a duration of 2 h, the AgNPs/MCFA exhibited superior antibacterial effectiveness against *E. coli* and *S. aureus*, demonstrating inhibition zones measuring 23

 doi:10.20944/preprints202507.0483.v1

mm and 22 mm, respectively. However, excessively high temperatures coupled with prolonged exposure may lead to oxidation of AgNPs [37], consequently reducing their antibacterial efficacy.

2.4. The MIC of AgNPs/MCFA

The minimum inhibitory concentration (MIC) is defined as the lowest concentration of an antimicrobial agent that prevents the visible growth of a microorganism when cultured at a specific temperature for 18 h. A lower MIC value indicated greater susceptibility of the microorganism to the antimicrobial agent, thereby reflecting enhanced antibacterial activity [38]. As shown in Table 1, when the concentration of AgNPs/MCFA was equal to or exceedsed 2 $mg \cdot mL^{-1}$, it demonstrated inhibitory effects on both *E. coli* and *S. aureus*, as evidenced by the clarification of the bacterial suspension in the test tube. The MIC values for *E. coli* and *S. aureus* were determined to be 0.5 $mg \cdot mL^{-1}$ and 2 $mg \cdot mL^{-1}$, respectively. These findings indicated that AgNPs/MCFA can effectively suppress the growth of both bacteria in aqueous solution. Notably, a higher concentration of AgNPs/MCFA was required to inhibit *S. aureus* compared to *E. coli*, suggesting stronger antibacterial efficacy against *E. coli*. This observation aligned with the results obtained from experiments assessing antibacterial zone.

Table 1. Determination of MIC value of AgNPs/MCFA.

No.	Concentration ($mg \cdot mL^{-1}$)	Tested bacteria	
		E. coli	*S. aureus*
1	64	–	–
2	32	–	–
3	16	–	–
4	8	–	–
5	4	–	–
6	2	–	–
7	1	–	+
8	0.5	–	+
9	0.25	+	+

Note: "+" result signifies that the test tube exhibits turbidity with visible bacterial growth; "—" result indicates that the test tube is clear with no observable bacterial growth.

2.5. Impact of AgNPs/MCFA on Bacterial Nucleic Acid Leakage, Protein Leakage and Electrical Con Ductivity

The disruption of the bacterial cell membrane is accompanied by the leakage of intracellular contents. The impact of AgNPs/MCFA on this leakage can be quantified by measuring the optical density or specific components presented in the supernatant of the bacterial culture medium. As shown in the Figure 2, AgNPs/MCFA exertsed varying effects on the membrane integrity of *E. coli* and *S. aureus*, with distinct levels of impact observed. From the perspective of protein leakage, it was noted that the soluble protein content progressively increased with extended culture time. Moreover, an increase in AgNPs/MCFA concentration resulted in a significant elevation in soluble protein levels compared to those observed in the control group. Remarkably, AgNPs/MCFA showed a greater destructive effect on the cell membrane of *E. coli*, leading to a rapid rise in soluble protein levels during the final 2 h of culture. Ultimately, an AgNPs/MCFA concentration of 1/2 MIC showed enhanced destructive effects on both *E. coli* and *S. aureus* cell membranes, resulting in increased leakage of soluble proteins. In terms of nucleic acid leakage, its trend over time closely mirrored that observed for protein leakage as culture duration extended.

After bacterial lysis, the release of intracellular K^+, Ca^{2+} and other ions into the extracellular environment can be monitored [39]. This phenomenon can be quantified by measuring electrical

 doi:10.20944/preprints202507.0483.v1

conductivity, thus enabling an assessment of the extent membrane damage. The electrical conductivity in the control group showed minimal variation. As the concentration of AgNPs/MCFA increased, cell membrane damage intensified, leading to a corresponding rise in measured conductivity. Over time, the conductivity of *E. coli* and *S. aureus* initially increased and then decreased, reaching peak values at 6 and 8 h, respectively. The initial increase in conductivity may be attributed to cell membrane damage leading to cell leakage. However, as time progressed, the rate of charge flow within the bacteriostatic solution diminished, ultimately culminating in complete destruction of the cell membrane and a subsequent decline in conductivity.

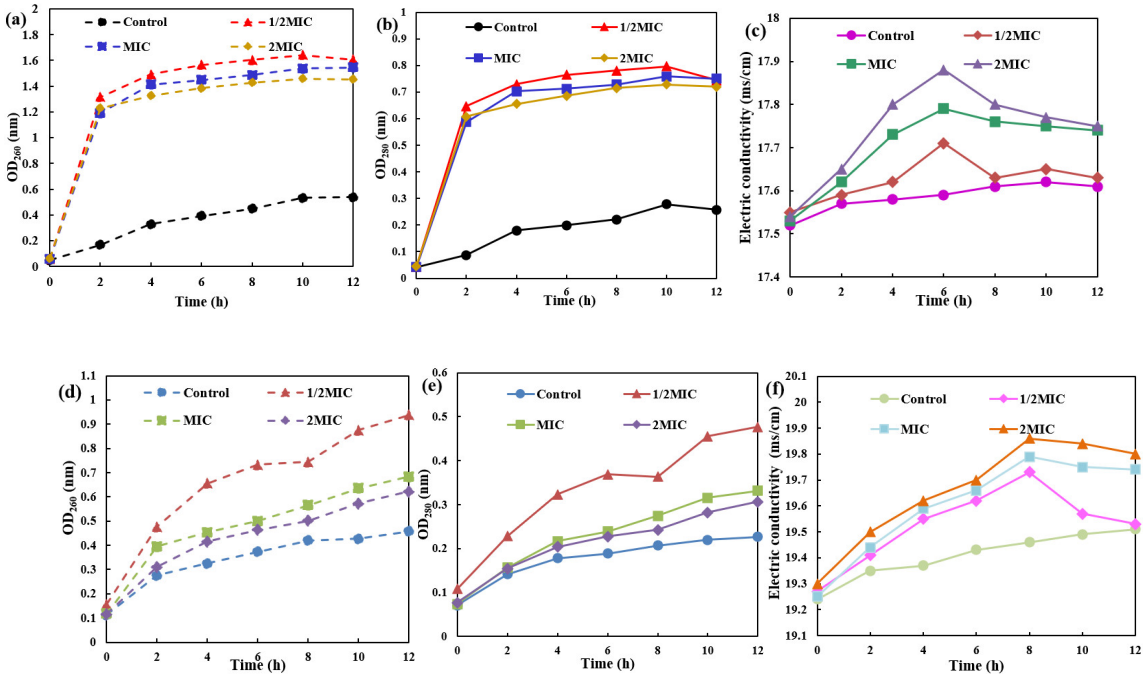

Figure 2. Nucleic acid, protein and electrolyte leakage from *E. coli* (a, b, c) and *S. aureus* (d, e, f).

2.6. Antimicrobial Kinetics

Different amounts of AgNPs/MCFA were introduced into culture media inoculated with *E. coli* and *S. aureus*, as shown in Figure 3 The optical density (OD) at 600 nm (OD_{600}) was measured to monitor bacterial growth, where higher values indicate microbial density. The results revealed a concentration-dependent reduction in OD_{600} with escalating levels of AgNPs/MCFA, suggesting a pronounced inhibitory effect on bacterial proliferation. Studies confirmed that AgNPs/MCFA effectively suppress the growth of both *E. coli* (Gram-negative) and *S. aureus* (Gram-positive), without significant differences in efficacy between the two bacterial types. This broad-spectrum activity may arise from AgNPs/MCFA targeting common bacterial structures, such as cell membranes or energy metabolism, rather than strain-specific components. These findings underscored the potential of AgNPs/MCFA as an effective antibacterial agent in aqueous environments, thereby supporting its development for nano-silver-based aquatic antimicrobial applications.

 doi:10.20944/preprints202507.0483.v1

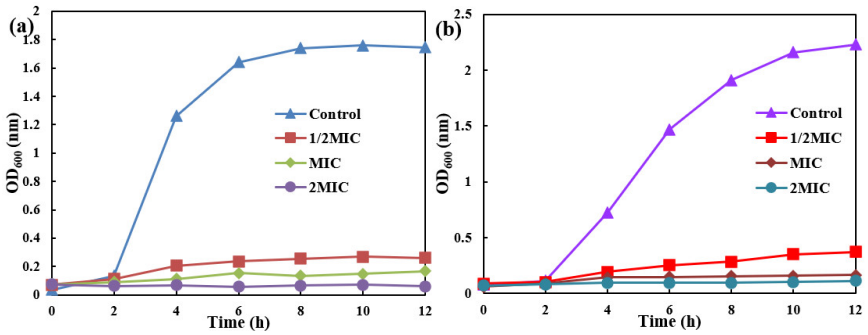

Figure 3. The growth of *E. coli* (a) and *S. aureus* (b) under different MIC concentrations of AgNPs/MCFA.

2.7. Catalytic Performance of AgNPs/MCFA for Degradation of MO

Figure 4 depicted the kinetic fitting curve for MO degradation catalyzed by AgNPs/MCFA produced at different $AgNO_3$ concentrations, sintering temperature, and sintering time. The results showed that MO degradation followed first-order kinetics, as evidenced by the strong linear correlation observed in the kinetic fitting curves. At lower AgNPs concentrations, insufficient synthesis led to a limited number of catalytic active sites, resulting in reduced efficiency in MO degradation due to insufficient electron mediation [40]. Conversely, overproduction of AgNPs can lead to aggregation and the formation of larger particles, thereby reducing the effective catalytic surface area and obstructing active sites, ultimately reducing catalytic efficiency.

Furthermore, the accessible surface area was limited at lower sintering temperature due to the underdeveloped pore structure. As a result, hydroxyl groups (-OH) were not properly exposed, diminishing the number of binding sites for AgNPs and slowing down the kinetics of MO degradation. Conversely, high-temperature sintering posed a risk of pore collapse, leading to a reduction in total surface area. This phenomenon significantly decreased the interaction between CFA and AgNPs by promoting the consolidation of AgNPs into larger particles through processes such as Ostwald ripening or coalescence [41]. Such aggregation reduced the number of active sites available and disrupts their uniform distribution.

Similarly, the duration of sintering was crucial. Insufficient sintering time failed to completely remove residual carbon and water from CFA, leading to a reduced specific surface area and incomplete exposure of hydroxyl groups (Si-OH) as well as defect sites in silica-aluminum oxides. Appropriately extending the sintering time enhanced the crystallinity of AgNPs, promoting an orderly atomic arrangement and enhancing both thermal and chemical stability of the material. However, excessive sintering time resulted in pronounced grain growth, diminishing surface activity.

By systematically optimizing the sintering temperature and duration, the synergistic interaction between CFA and AgNPs, termed "carrier-active site", can be maximized, thereby significantly enhancing the catalytic degradation efficiency of MO. Consequently, the highest rate constant k_a value was achieved for AgNPs/MCFA prepared under conditions of 0.5 $g \cdot L^{-1}$ $AgNO_3$ concentration, 250 °C and a duration of 2 h (Table S1) indicating the optimal catalytic degradation rate of MO. To quantify this effect, we introduced a normalized activity parameter defined as the ratio of rate constant k_a to the total mass of the catalyst (m), k' (k'=k/m). The catalytic activity parameter for AgNPs/MCFA in reducting MO was obtained to be 6.2 $min^{-1} \cdot g^{-1}$. Therefore, AgNPs/MCFA served as an effective catalyst for degrading organic dyes and held significant potential for application in wastewater treatment.

 doi:10.20944/preprints202507.0483.v1

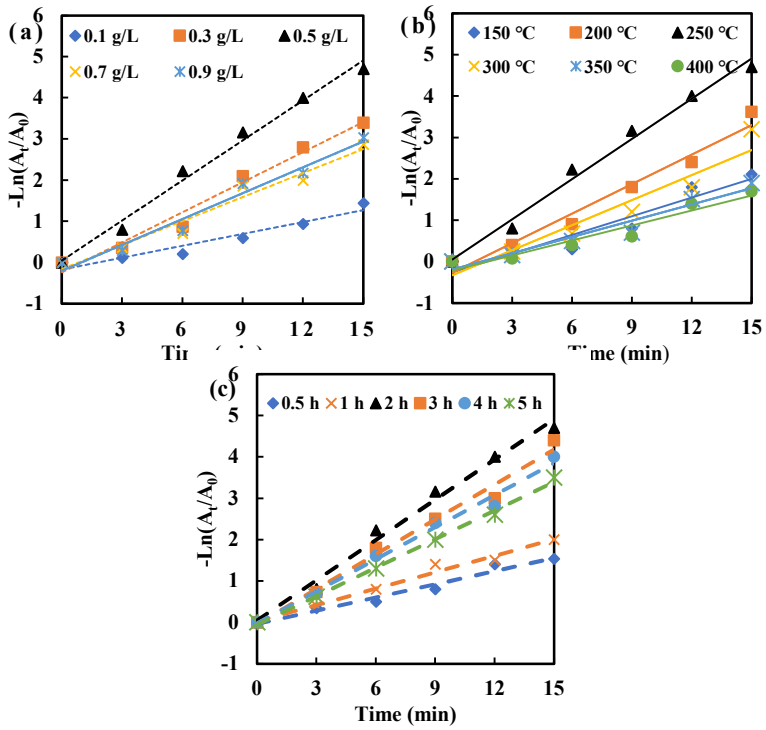

Figure 4. Kinetic model of MO degradation under different preparation conditions ($AgNO_3$ concentration (a), sintering temperature (b) and sintering time (c)).

3.8. Reusability of AgNPs/MCFA

Reusability is a critical indicator of material quality. The capacity to maintain high antimicrobial efficacy and degradation rates after undergoing multiple testing cycles contributed significantly to reducing application costs. Furthermore, to eliminate impurities, the particles were sequentially treated with alcohol and water. After being used continuously for five cycles, they still exhibited commendable antibacterial properties and degradability, as shown in Figure 5. This further demonstrated that through in-situ synthesis, AgNPs can be more effectively immobilized on CFA, thereby minimizing leaching and migration. AgNPs/MCFA can be employed to eliminate harmful microorganisms and toxic contaminants from water. However, its recyclability and reusability in water treatment processes were of critical importance. A notable advantage of AgNPs/MCFA over other nanoparticles lies in its ability to be easily separated from water by applying an external magnetic field. This facilitated the recovery of particles following each treatment cycle, thus minimizing the potential release of nanoparticles into the environment.

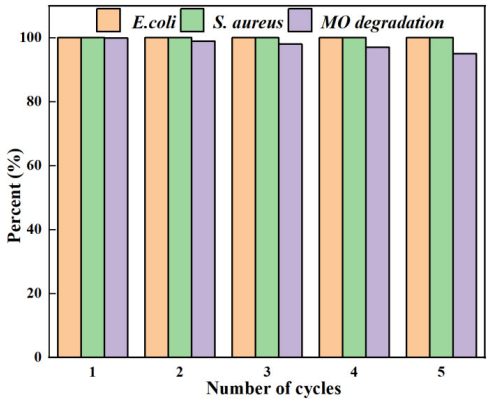

Figure 5. Antibacterial and MO degradation of AgNPs/MCFA recycling for 5 times.

 doi:10.20944/preprints202507.0483.v1

3.9. Proposed Antibacterial and Degradation Mechanism of AgNPs/MCFA

After acid treatment, the surface morphology of CFA transitions from a smooth to a rough texture, resulting in an increase in porosity, specific surface area, and physical adsorption capacity. This micrometer-scale pore structure facilitated bacterial adsorption and enhanced accessibility for AgNPs, ultimately leading to the damage to microbial cells. AgNPs inherently possessed a positive charge, which enabled effective electrostatic adsorption with negatively charged bacterial cell walls. Upon disrupting these cell walls and membranes, AgNPs directly interacted with intracellular DNA, compromising its normal structure and physiological function through specific interactions with the outer-ring nitrogen atoms found in bases such as adenine and pyrimidine. Furthermore, AgNPs can engage with and inactivate disulfide bonds and sulfhydryl groups within enzymes responsible for cellular metabolism, particularly respiratory enzymes, thereby generating reactive oxygen species (ROS) that induced oxidative stress in microorganisms. This process results in the loss of active intracellular electrolytes (e.g., K^+, Ca^{2+}, Cl^-, and PO_4^{3-}), nucleic acids, and proteins. these components were subsequently released into extracellular solutions (Figure 6 (a)). Consequently, measurements of solution conductivity (ion leakage), along with OD_{260} (nucleic acid release) and OD_{280} (protein release) absorbance, in cultures treated with varying MIC levels of AgNPs/MCFA, provide robust confirmation of membrane disruption and cellular content leakage. Moreover, Gram-positive bacteria (e.g., *S. aureus*) exhibit significantly higher resistance to AgNPs compared to Gram-negative bacteria (e.g., *E. coli*). This disparity in susceptibility can be attributed to fundamental differences in cell envelope structure. Specifically, the dense peptidoglycan layer in Gram-positive organisms may limit nanoparticle penetration and subsequent intracellular damage.

After acid treatment, the surface properties of CFA not only improved but also exhibited a positive charge characteristic. This facilitated strong electrostatic adsorption with dye anions in water, thereby enhancing the adsorption performance of CFA. Although $NaBH_4$ was a powerful reducing agent, its aqueous solution failed to effectively reduce MO due to the substantial difference in redox potential between MO and $NaBH_4$. Consequently, these reactions were kinetically hindered despite being thermodynamically feasible. The interaction between MO and $NaBH_4$ can be classified as an electron transfer process, wherein $NaBH_4$ served as the electron donor while MO functioned as the electron acceptor [42]. AgNPs/MCFA served as an effective intermediary for the H^- ions released during the interaction between MO and $NaBH_4$, thus promoting efficient electron transfer. The presence of AgNPs accelerated the reduction reactions owing to their large surface area. Prior to reduction, both reactants were adsorbed onto the surface of AgNPs/MCFA. Acid-treated CFA demonstrated enhanced surface characteristics with positively charged properties, which facilitated this process by attracting reactants to the AgNPs/MCFA surface through electrostatic interactions. Subsequently, H^- ions transferred electrons to the AgNPs/MCFA surface, enabling MO molecules to accept electrons. This weakened the azo double bond (-N=N-), thereby driving the color degradation react (Figure 6 (b)).

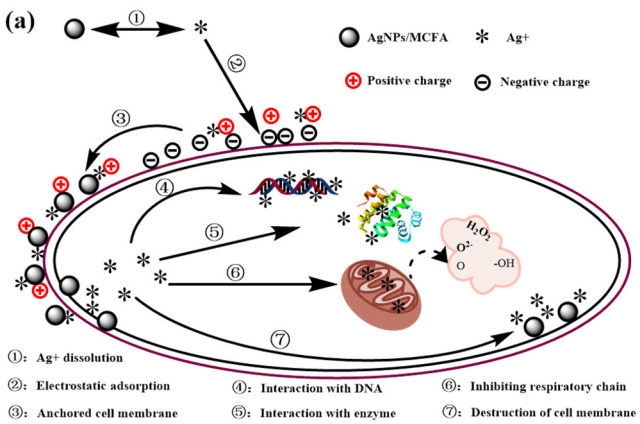

 doi:10.20944/preprints202507.0483.v1

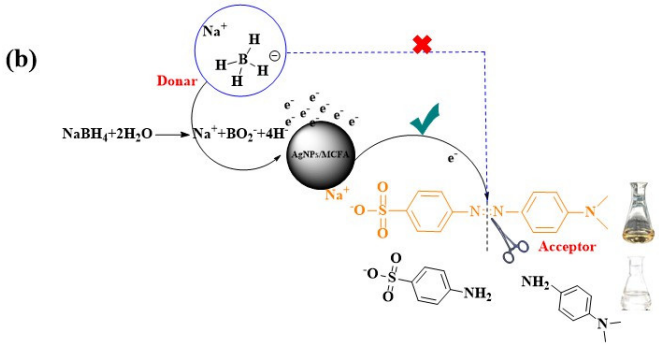

Figure 6. Mechanism of AgNPs/MCFA-induced damage to bacterial cells(a) and reductive degradation of MO(b).

3. Materials and Methods

3.1. Chemicals and Bacteria

Coal fly ash (CFA, 5000 mesh) was procured from Henan Borun Casting Material Co., Ltd. (Henan, China). Sodium borohydride was obtained from Shanghai Lingfeng Chemical Reagent Co., LTD. (Shanghai, China).MO, $AgNO_3$, $FeCl_3$, $FeSO_4$ and sodium citrate ($C_6H_5Na_3O_7$) were sourced from Sinopharm Group Chemical Reagent Co., LTD. (Shanghai, China). Peptone, yeast extract, agar and NaCl were acquired from Fuchen Chemical Reagent Co., LTD. (Tianjin, China). *Escherichia coli* (*E. coli*) was selected as a representative strain of Gram-negative bacteria and *Staphylococcus aureus* (*S. aureus*) as a representative strain of Gram-positive bacteria. *Escherichia coli* (ATCC 25922) and *Staphylococcus aureus* (ATCC 6538) were procured from China Center of Industrial Culture Collection.

3.2. Preparation of Composite Materials

3.2.1. Magnetization of CFA

The CFA was stirred in a 10 wt% HCl solution at 90 °C for 1 h, followed by filtration and washing to neutral pH, and then dried to obtain acidified CFA. Subsequently, a mixed solution was prepared by combining equal volumes of 0.012 mol·L^{-1} $FeCl_3$ with 0.005 mol·L^{-1} $FeSO_4$. The acidified CFA was introduced into the mixed solution, which was then heated to 70 °C on a magnetic stirrer, and the pH of the solution was adjusted to 8–9 using 1 mol·L^{-1} NaOH. The beaker was then subjected to ultrasonic treatment for 30 min to achieve ultrasonic dispersion. Following this, the mixture was aged for an additional hour. Finally, the precipitate was filtered out, washed until it reached a neutral pH, and dried to obtain magnetic CFA (MCFA).

3.2.2. Preparation of AgNPs/MCFA

The MCFA was immersed in $AgNO_3$ solutions of varying concentrations (0.1, 0.3, 0.5, 0.7, and 0.9 g·L^{-1}) under dark conditions with continuous stirring for 2 h. After that, an appropriate amount of sodium citrate was added as a reducing agent, and the mixture was stirred for 24 h to promote the formation of AgNPs. Finally, the AgNPs-loaded MCFA was filtered, washed, and dried. The dried sample was sintered in a tube furnace under an inert atmosphere with a controlled heating rate of 10 °C·min^{-1} to specific sintering temperatures (150, 200, 250, 300, 350, and 400 °C), with a sintering time (0.5, 1, 2, 3, 4, and 5 h) maintained throughout the process. After allowing the sample to cool naturally, it was ground to obtain the final product, AgNPs/MCFA.

3.3. Characterization of Materials

Scanning electron microscopy (SEM, Hitachi Regulus 8100, Japan) and transmission electron microscopy (TEM, FEI Talos F200X, USA) characterized the surface morphology and microstructure of the materials. Fourier transform infrared spectroscopy (FT-IR, Thermo Fisher Scientiffc, USA) was

 doi:10.20944/preprints202507.0483.v1

employed to investigate the functional groups and chemical bonds in the range of 500 cm^{-1} to 4000 cm^{-1}. X-ray diffraction (XRD, Smart Lab SE, Tokyo, Japan) was utilized to characterize the mineralogical composition and phase structure. Value Stream Mapping (VSM, Lakeshore 7404, USA) was used to obtain the saturation magnetization of material.

3.4. Determination of the Antibacterial Activity of AgNPs/MCFA

3.4.1. Size of the Antibacterial Zone

Typically, bacteria exhibit uniform growth on agar media. Nevertheless, in the presence of antimicrobial materials, the antimicrobial components diffuse into specific regions of the medium, impeding bacterial growth and creating an inhibition zone. Notably, the larger the relative area of this inhibition zone, the more potent the antibacterial effect. The colonies of *E. coli* and *S. aureus* were selected and cultivated in LB liquid medium (comprising 10 $g{\cdot}L^{-1}$ peptone, 5 $g{\cdot}L^{-1}$ yeast extract, and 10 $g{\cdot}L^{-1}$ sodium chloride) at 37 °C. Upon reaching a measured concentration of viable bacteria at $1.0{\times}10^{8}$ $CFU{\cdot}mL^{-1}$, 0.1 mL of *E. coli* and *S. aureus* was separately inoculated onto LB solid medium (containing10 $g{\cdot}L^{-1}$ peptone, 5 $g{\cdot}L^{-1}$ yeast extract, 10 $g{\cdot}L^{-1}$ sodium chloride, and 20 $g{\cdot}L^{-1}$ agar). After flame sterilization, a 9.0 mm round hole was drilled in the plate with a hole puncher, and then 0.1 g of the aforementioned AgNPs/MCFA composite was filled into the hole and finally cultured at 37 °C incubator for 18 h. The diameter of the resulting antibacterial zone for each sample was then measured in millimeters to assess its effectiveness against the respective bacterial strains present on the plate.

3.4.2. Minimum Inhibitory Concentration (MIC)

The MIC of the AgNPs/MCFA composite was determined using the double gradient dilution method [27], with sterile distilled water employed for the gradient dilution. *E. coli* and *S. aureus* were cultured to the logarithmic phase and diluted into the LB medium at a concentration of $1.0{\times}10^{8}$ $CFU{\cdot}mL^{-1}$. Specifically, the bacterial solution ($1.0{\times}10^{8}$ $CFU{\cdot}mL^{-1}$) was added to each sterile centrifuge tubes numbered from 1 to 9. Each tube received 1 mL of the bacterial solution, except for tube 1, which was filled with 1.8 mL. Subsequently, 0.2 mL of the AgNPs/MCFA composite suspension was added to initial tube, thoroughly mixed, and then transferred by dilution in increments of 1 mL from one tube to the next in sequence until reaching the ninth tube. Finally, 1 mL of the solution was discarded from the ninth tube. All samples were placed in a thermostatic oscillator and incubated at 37 °C for 18 h. The MIC value was defined as the lowest concentration at which no turbidity was visible upon visual inspection.

3.4.3. Nucleic Acid, Protein Leakage and Electrical Conductivity

E. coli and *S. aureus* were cultured to a concentration of $1.0{\times}10^{8}$ $CFU{\cdot}mL^{-1}$. The bacterial cells were harvested by centrifugation at 5000 rpm for 30 min. After centrifugation, the cells were washed twice with normal saline. The washed cell pellets were resuspended in saline until the optical density at a wavelength of 600 nm (OD_{600}) of the suspension reached 0.6. The bacterial suspensions were then treated with the AgNPs/MCFA composite at concentrations equivalent to 2 times the minimum inhibitory concentration (2MIC), the minimum inhibitory concentration (MIC), and half of the minimum inhibitory concentration (0.5MIC). These mixtures were incubated in a thermostatic shaker at 37 °C for 12 h. During the incubation process, 2 mL aliquots were taken out every 2 h for analysis. The absorbance of the bacterial suspensions was measured at 260 nm (nucleic acid release) and 280 nm (protein release), in order to evaluate the cellular leakage. The electrical conductivity (ion leakage) of the suspensions was determined using a conductivity meter (Shanghai Yi Dian Scientific Instruments Co., Ltd., China). For all the measurements, bacterial suspensions that did not contain the AgNPs/MCFA composite were used as blank controls.

3.4.4. Antimicrobial Kinetics

 doi:10.20944/preprints202507.0483.v1

E. coli and *S. aureus* were cultured to a concentration of 1.0×10^8 CFU·mL^{-1}, and 1.0 mL of each bacterial suspension was inoculated into 100 mL of LB medium. The AgNPs/MCFA composite, which had been diluted with sterile water, was introduced at final concentrations corresponding to 2MIC, MIC, and 0.5MIC. The cultures were then incubated in a thermostatic shaker at 37 °C for 12 h. During the incubation period, 2 mL aliquots were taken out every 2 h, and the absorbance at 600 nm was measured using a UV-vis spectrophotometer (Shanghai Yi electric Analytical Instrument Co., LTD, Shanghai, China) to plot the antibacterial kinetics curve. A control group, devoid of any AgNPs/MCFA composite, was maintained under identical conditions for comparison.

3.5. The Catalytic Efficiency of AgNPs/MCFA

The catalytic activity of AgNPs/MCFA composite was assessed in the reduction reaction of MO, which served as a model dye, with $NaBH_4$ acting as the reducing agent. In a typical experiment, 100 mL of MO (100 mg·L^{-1}) and 2 mL of $NaBH_4$ (0.2 mol·L^{-1}) were combined in a 250 mL conical flask, and 50 mg of the AgNPs/MCFA composite was placed on a magnetic stirrer at 30 °C. At specific time intervals, 2 mL of the reaction mixture was taken out. Subsequently, UV-visible spectrophotometry was used to monitor the degradation of MO at its maximum absorbance peak (OD_{465}). After the reaction had proceeded for15 min, the degradation rate (R) was calculated using the following formula:

$$R(\%) = \frac{C_0 - C_t}{C_0} \times 100 \qquad (1)$$

C_0 and C_t indicate the mass concentration of the dye at the beginning and t, respectively (mg·L^{-1}).

Generally, the reduction reaction can be assumed as a pseudo-first-order kinetics due to excess concentration of $NaBH_4$ compared to MO. It can be described by Langmuir-Hinshelwood equation [28].

$$\ln\left(\frac{A_t}{A_0}\right) = -k_a t \qquad (2)$$

where, A_0 and A_t indicate the absorbance value of the dye at the beginning and t, respectively; k_a is the reaction rate constant (min^{-1}).

3.6. Reusability of AgNPs/MCFA

The reusability of AgNPs/MCFA composite is a crucial parameter for evaluating its performance [29]. After each application, the AgNPs/MCFA composite was retrieved and thoroughly washed with alcohol and deionized water, dried and then utilized for subsequent antibacterial and MO dye degradation experiments. The bacteriostatic rate and dye degradation rate were employed to evaluate the efficacy of each experiment.

The number of colonies in the original bacterial solution and the number of colonies after inhibition were determined by the plate counting method. Based on the data obtained, the antibacterial rate of the AgNPs/MCFA composite was calculated according to the following formula.

$$Antibacterial\ rate(\%) = \frac{N_0 - N}{N_0} \times 100 \qquad (3)$$

N_0 is the initial colony number, N is the number of colonies after inhibition.

The reusability experiment of the AgNPs/MCFA composite in dye degradation was conducted following the same procedure as described in Section 3.5.

4. Conclusion

In summary, AgNPs/MCFA composite developed in this study combined potent antibacterial activity against both Gram-negative (*E. coli*) and Gram-positive (*S. aureus*) bacteria with excellent catalytic performance for the degradation of the azo dye MO. Its magnetic recoverability and reusability further enhance its practical applicability in wastewater treatment. This study provided a robust foundation for developing low-cost, multifunctional materials for sustainable wastewater treatment, aligning with global priorities for circular economy and green chemistry.

 doi:10.20944/preprints202507.0483.v1

Supplementary Materials: The following supporting information can be downloaded at the website of this paper posted on Preprints.org, Figure S1: The SEM image of CFA (a), MCFA (b), and AgNPs/MCFA (c); Figure S2: The TEM image of AgNPs/MCFA; Figure S3: The FTIR spectrum of CFA (a), MCFA (b), and AgNPs/MCFA (c); Figure S4: The XRD pattern of CFA (a), MCFA (b), and AgNPs/MCFA (c); Figure S5: The VSM image of Fe_3O_4 (a), AgNPs/MCFA (b); Table S1: Parameters and regression coefficients for the kinetic model and degradation rate.

Author Contributions: Conceptualization, Lei Gong; methodology, Lei Gong and Jiaxin Li; software, Lei Gong and Rui Jin; validation, Lei Gong, Jiaxin Li and Rui Jin; formal analysis, Lei Gong and Menghao Li; investigation, Lei Gong and Jiaxin Li; resources, Lei Gong; data curation, Lei Gong and Jiajie Peng; writing—original draft preparation, Lei Gong; writing—review and editing, Jie Zhu; visualization, Menghao Li and Jiajie Peng; supervision, Jie Zhu; project administration, Lei Gong and Jie Zhu. Funding acquisition, Lei Gong. All authors have read and agreed to the published version of the manuscript.

Funding: This research was funded by the Project of Natural Science Research in Universities of Jiangsu Province (22KJB530004) and National Natural Science Foundation of China (22208030).

Institutional Review Board Statement: Not applicable.

Informed Consent Statement: Not applicable.

Data Availability Statement: All data supporting the findings of this study are available within

the paper.

Conflicts of Interest: The authors declare no conflicts of interest.

Abbreviations

The following abbreviations are used in this manuscript:

MCFA	magnetized coal fly ash
AgNPs	silver nanoparticles
MO	methyl orange
CFA	coal fly ash
MIC	minimum inhibitory concentration
ROS	reactive oxygen species

References

1. Ma, H.D.; Yu, L.J.; Yang, L.M.; Yao, Y.J.; Shen, G.D.; Wang, Y.Z.; Li, B.; Meng, J.G.; Miao, M.H.; Zhi, C. Graphene oxide composites for dye removal in textile, printing and dyeing wastewaters: a review. *Environ. Chem. Lett.*, **2025**, *23*, 165-193. DOI:10.1007/s10311-024-01794-4
2. Song, J.T.; Chen, S.F.; Lyu, R.; Zhang, D.H.; Hong, J.P. Facile synthesis of hyperbranched magnetic nanospheres for highly efficient removal of methyl orange. *New J. Chem.*, **2024**, *48*, 9945-9953. DOI:10.1039/d4nj00423j
3. Dai, J.Z.; Wu, Y.H.; Yao, Y.H.; Zhang, B. ZnO/TiO_2 photocatalysts for degradation of methyl orange by low-power irradiation. *Sci. Progress*, **2025**, *108*, 1-25. DOI:10.1177/00368504251322606
4. Xue, S.H.; Lin, P.Y.; Pang, Y.X.; Li, Z.X.; Zhou, M.S.; Qiu, X.Q.; Lou, H.M. A composite of AgNPs and lignin porous microspheres via in-situ reduction of Ag^+ and its catalytic performance. *Int. J. Biol. Macromol.*, **2024**, *273*, 132899. DOI:10.1016/j.ijbiomac.2024.132899
5. Fatima, I.; Ajmal, M.; Naseem, A.; Ali, A.; Javed, F.; Hashmi, M.A.; Mahmood, K.; Ahmad, M.; Ullah, F.; Ahmad, Z. Fabrication of efficient and easily recyclable silver nanoparticles-anionic polymer hydrogel composite catalyst for rapid degradation of water pollutants. *J. Appl. Polym. Sci.*, **2025**, *142*, e56841. DOI:10.1002/app.56841
6. Ghasemi, M.; Govahi, M.; Litkohi, H.R. Green synthesis of silver nanoparticles (AgNPs) and chitosan-coated silver nanoparticles (CS-AgNPs) using *Ferula gummosa Boiss gum* extract: A green nano drug for

 doi:10.20944/preprints202507.0483.v1

potential applications in medicine. *Int. J. Biol. Macromol.*, **2025**, *291*, 138619. DOI:10.1016/j.ijbiomac.2024.138619

7. Lu, F.F.; Liu, Y.X.; Dai, Y.X.; Zhang, G.X.; Tong, Y.N. Preparation of nanosilver/polymer composites and evaluation of their antimicrobial and antitumor effect. *RSC Adv.*, **2025**, *15*, 6357-6369. DOI:10.1039/d4ra08108k
8. Singh, J.; Perumal, V.; Singh, U.; Tripathi, D.K.; Sharma, S. Green synthesis of silver nanoparticles from bark extract of Terminalia arjuna and their application as next generation antibacterial agents. *Curr. Nanosci.*, **2022**, *18*, 743-757. DOI:10.2174/1573413718666220221102909
9. Korkmaz, N.; Ceylan, Y.; İmamoğlu, R.; Kısa, D.; Şen, F.; Karadağ, A. Eco-friendly biogenic silver nanoparticles: synthesis, characterization and biological applications. *Int. J. Environ. Sci. Te.*, **2024**, *22*, 3707-3716. DOI:10.1007/s13762-024-05860-w
10. Eslam, I.E.; Seleem, E.G.; Moustafa, M.Z.; Abdelaleem, H.A. Characterization of biosynthesized silver nanoparticles by *Haplophyllum tuberculatum* plant extract under microwave irradiation and detecting their antibacterial activity against some wastewater microbes. *Desalin Water Treat.*, **2020**, *195*, 275-285. DOI:10.5004/dwt.2020.25876
11. Zheng, L.Q.; Yu, X.D.; Xu, J.J.; Chen, H.Y. Reversible catalysis for the reaction between methyl orange and $NaBH_4$ by silver nanoparticles. *Chem. Commun.*, **2015**, *51*, 1050-1053. DOI:10.1039/c4cc07711c
12. Kebir-Medjhouda, A.Z.; Abdelkrim, S.; Zahraoui, M.; Mokhtar, A.; Maloufi, M.; Belkadi, A.; Djelad, A.; Belarbi, H.; Boukoussa, B.; Hasnaoui, M.A.; Sassi, M. Preparation and characterization of silver nanoparticles-magadiite materials. Application to reduction of toxic organic dyes. *Silicon*, **2023**, *15*, 3767-3781. DOI:10.1007/s12633-023-02377-8
13. Gil-Korilis, A.; Cojocaru, M.; Berzosa, M.; Gamazo, C.; Andrade, N.J.; Ciuffi, K.J. Comparison of antibacterial activity and cytotoxicity of silver nanoparticles and silver-loaded montmorillonite and saponite. *Appl. Clay Sci.*, **2023**, *240*, 106968. DOI:10.1016/j.clay.2023.106968
14. Altintig, E.; Sarici, B.; Karatas, S. Prepared activated carbon from hazelnut shell where coated nanocomposite with Ag^+ used for antibacterial and adsorption properties. *Environ. Sci. Pollut. R.*, **2023**, *30*, 13671-13687. DOI:10.1007/s11356-022-23004-w
15. Nagaraj, K.; Thankamuniyandi, P.; Kamalesu, S.; Lokhandwala, S.; Lokhandwala, S.; Sakthinathan, S.; Chiu, T.; Karuppiah, C. Green synthesis, characterization and efficient photocatalytic study of hydrothermal-assisted Ag@TiO_2 nanocomposites. *Inorg. Chem. Commun.*, **2023**, *148*, 110362. DOI:10.1016/j.inoche.2022.110362
16. Mushtaq, F.; Zahid, M.; Bhatti, I.A.; Nasir, S.; Hussain, T. Possible applications of coal fly ash in wastewater treatment. *J. Environ. Manage.*, **2019**, *240*, 27-46. DOI:10.1016/j.jenvman.2019.03.054
17. Chen, Y.; Fan, Y.J.; Huang, Y.; Liao, X.L.; Xu, W.F.; Zhang, T. A comprehensive review of toxicity of coal fly ash and its leachate in the ecosystem. *Ecotox. Environ. Safe.*, **2024**, *269*, 115905. DOI:10.1016/j.ecoenv.2023.115905
18. Wang, S.Z.; Baxter, L. Comprehensive study of biomass fly ash in concrete: Strength, microscopy, kinetics and durability. *Fuel Process. Technol.*, **2007**, 88, 1165-1170. DOI:10.1016/j.fuproc.2007.06.016
19. Ge, J.C.; Yoon, S.K.; Choi, N.J. Application of fly ash as an adsorbent for removal of air and water pollutants. *Appl. Sci-Basel*, **2018**, *8*, 1116. DOI:10.3390/app8071116
20. Yang, J.L.; Zhao, L.; Zhou, T.R.; Ma, S.H.; Wang, X.H. Catalytic oxidation activity of NO over mullite-supported amorphous manganese oxide catalyst. *Materials*, **2023**, *16*, 3821. DOI:10.3390/ma16103821
21. Malpani, S.K.; Goyal, D.; Katara, S.; Rani, A. Green, efficient and economical coal fly ash based phosphomolybdic acid catalysts: preparation, characterization and application. *Chem. Pap.*, **2021**, *75*, 3017-3034. DOI:10.1007/s11696-020-01501-x
22. Ge, J.C.; Kim, J.Y.; Yoon, S.K.; Choi, N.J. Fabrication of low-cost and high-performance coal fly ash nanofibrous membranes via electrospinning for the control of harmful substances. *Fuel*, **2019**, *237*, 236-244. DOI:10.1016/j.fuel.2018.09.068
23. Chen, Y.J.; Chen, R.F.; Chang, X.L.; Yan, J.Y.; Gu, Y.J.; Xi, S.; Sun, P.F.; Dong, X.P. Ozone catalysis degradation of sodium acetate via vacancy-driven radical oxidation over Fe-modified fly ash. *Water*, **2023**, *15*, 3801. DOI:10.3390/w15213801

 doi:10.20944/preprints202507.0483.v1

24. Rodwihok, C.; Suwannakeaw, M.; Charoensri, K.; Wongratanaphisan, D.; Woo, S.W.; Kim, H.S. Alkali/zinc-activated fly ash nanocomposites for dye removal and antibacterial applications. *Bioresource Technol.*, **2021**, *331*, 125060. DOI:10.1016/j.biortech.2021.125060
25. Ma, Y.; Zhao, Z.H.; Fan, J.M.; Gu, Z.Y.; Zhang, B.; Yin, S. Ag-TON nanospheres coupled with fly ash cenospheres for wastewater treatment under visible light irradiation. *Water Sci. Technol.*, **2018**, *78*, 2321-2327. DOI:10.2166/wst.2018.513
26. Subramanian, E.; Subbulekshmi, N.L. Enhanced heterogeneous wet hydrogen peroxide catalytic oxidation performance of fly ash-derived zeolite by CuO incorporation. *Sci. Iran.*, **2017**, *24*, 1189-1202. DOI:10.24200/sci.2017.4100
27. Mahmoud, R.; Kotb, N.M.; Gadelhak, Y.; El-Ela, F.I.A.; Shehata, A.Z.; Othman, S.I.; Allam, A.A.; Rudayni, H.A.; Zaher, A. Investigation of ternary Zn-Co-Fe layered double hydroxide as a multifunctional 2D layered adsorbent for moxifloxacin and antifungal disinfection. *Sci. Rep.*, **2024**, *14*, 806. DOI:10.1038/s41598-023-48382-0
28. Mohsen, M.; Towan, K.; Marjan, T.; Mohammad, T.Y.; Parnian, T.; Aseman, L. Facile green synthesis of silver nanoparticles using *Crocus Haussknechtii Bois bulb* extract: Catalytic activity and antibacterial properties. *Colloid Interfac. Sci.*, **2019**, *33*, 100211. DOI:10.1016/j.colcom.2019.100211
29. Ding, H.L.; Zhang, M.K.; Liu, Y.; Yao, Y.Z.; Mai, Z.H.; Zheng, H.X.; Song, B.; Fan, B.B.; Wang, H.L.; Lu, H.X. Synthesis of CS/Fe_3O_4/TiO_2@MXene nanocomposite photocatalyst with excellent degradation and bacteriostatic properties by one-step hydrothermal method. *Ceram. Int.*, **2024**, *50*, 46334-46346. DOI:10.1016/j.ceramint.2024.08.477
30. Dubnika, A.; Loca, D.; Rudovica, V.; Parekh, M.B.; Berzina-Cimdina, L. Functionalized silver doped hydroxyapatite scaffolds for controlled simultaneous silver ion and drug delivery. *Ceram. Int.*, **2017**, *43*, 3698-3705. DOI:10.1016/j.ceramint.2016.11.214
31. Chika, I.; Hritaal, S.; William, G.; Dominique, D.; Md., A.K.B.; Md., S.P.; Zmg, S.J.; Mohammed, M.R.; Faisal, I.C.; Jamal, U. Synthesis and characterization of silver nanoparticles and their promising antimicrobial effects. *Chem. Phys. Impact*, **2024**, *9*, 100758. DOI:10.1016/j.chphi.2024.100758
32. Linker, R.; Kenny, A.; Shaviv, A.; Singher, L.; Shmulevch, I. Fourier Transform Infrared-attenuated total reflection nitrate determination of soil pastes using principal component regression, partial least squares, and cross-correlation. *Appl. Spectrosc.*, **2004**, *58*, 516-520. DOI:10.1366/000370204774103327
33. Uda, M.N.A.; Gopinath, S.C.B.; Hashim, U.; Halim, N.H.; Parmin, N.A.; Uda, M.N.A.; Anbu, P. Production and characterization of silica nanoparticles from fly ash: conversion of agro-waste into resource. *Prep. Biochem. Biotech.*, **2021**, 51, 86-95. DOI:10.1080/10826068.2020.1793174
34. Liu, Y.; Liao, J.J.; Chang, L.P.; Bao, W.R. Ag modification of SBA-15 and MCM-41 mesoporous materials as sorbents of thiophene. *Fuel*, **2022**, *311*, 122537. DOI:10.1016/j.fuel.2021.122537
35. Gao, J.W.; Huang, Y.J.; Wang, S.; Zhu, Z.C.; Song, H.K.; Zhang, Y.Y.; Liu, J.; Qi, S.J.; Zhao, J.Q. Mineral transformation and solidification of heavy metals during co-melting of MSWI fly ash with coal fly ash. *Environ. Sci. Pollut. R.*, **2024**, 31, 45793-45807. DOI:10.1007/s11356-024-33827-4
36. Waldo-Mendoza, M.A.; Rivera-Garcia, N.A.; Robles-Martinez, M.; Mayorga-Colunga, P.C.; Martine-Montejano, R.C.; Perez, E. Effect of the interlayer distribution of ZnO decorated with Ag nanoparticles on the antimicrobial activity of multilayer poly(methyl methacrylate) films. *J. Vinyl Addit. Techn.*, **2024**, *30*, 1621-1634. DOI:10.1002/vnl.22146
37. Savvidou, M G; Kontari, E; Kalantzi, S; Mamma, D. Green synthesis of silver nanoparticles using the cell-free supernatant of *Haematococcus pluvialis* culture. *Materials*, **2024**, 17, 187. DOI:10.3390/ma17010187
38. Varghese, R.; Almalki, M.A.; Ilavenil, S.; Rebecca, J.; Choi, K.C. Silver nanopaticles synthesized using the seed extract of *Trigonella foenum-graecum L.* and their antimicrobial mechanism and anticancer properties. *Saudi J. Biol. Sci.*, **2019**, 26, 148-154. DOI:10.1016/j.sjbs.2017.07.001
39. Sulistyani, N.; Nurkhasanah; Angelita, L.; Rais, I.R.; Zakaria, Z.A. Role of flavonoid-rich fraction from *Persea americana* (Mill.) in bacterial leakage of *Staphylococcus aureus*. *Pak. J. Pharm. Sci.*, **2022**, *35*, 1805-1811. DOI:10.36721/PJPS.2022.35.6.SP.1805-1811.1
40. Seku, K.; Hussaini, S.S.; Hussain, M.; Siddiqui, M.A.; Golla, N.; Ravinder, D.; Reddy, G.B. Synthesis of *Frankincense gum* stabilized AgNPs by microwave irradiation and their catalytic, antioxidant, and

 doi:10.20944/preprints202507.0483.v1

antibacterial properties. *Physica E: Low-Dimensional Systems & Nanostructures*, **2022**, *140*, 115169. DOI:10.1016/j.physe.2022.115169

41. Behrens, M.A.; Franzén, A.; Carlert, S.; Skantze, U.; Lindfors, L.; Olsson, U. On the Ostwald ripening of crystalline and amorphous nanoparticles. *Soft Matter*, **2025**, *21*, 2349-2354. DOI:10.1039/d4sm01544d
42. Malik, A.; Nath, M. Synthesis of Ag/ZIF-7 by immobilization of Ag nanoparticles onto ZIF-7 microcrystals: A heterogeneous catalyst for the reduction of nitroaromatic compounds and organic dyes. *J. Environ. Chem. Eng.*, **2020**, *8*, 104547. DOI:10.1016/j.jece.2020.104547